

Mechanical Properties of Organic Electronic Polymers on the Nanoscale

Vishal Panchal, Illia Dobryden, Ude D. Hangen, Dimitrios Simatos, Leszek J. Spalek, Ian E. Jacobs, Guillaume Schweicher, Per M. Claesson, and Deepak Venkateshvaran*

Organic semiconducting polymers have attractive electronic, optical, and mechanical properties that make them materials of choice for large area flexible electronic devices. In these devices, the electronically active polymer components are micrometers in size, and sport negligible performance degradation upon bending the centimeter-scale flexible substrate onto which they are integrated. A closer look at the mechanical properties of the polymers, on the grain-scale and smaller, is not necessary in large area electronic applications. In emerging micromechanical and electromechanical applications where the organic polymer elements are flexed on length scales spanning their own micron-sized active areas, it becomes important to characterize the uniformity of their mechanical properties on the nanoscale. In this work, the authors use two precision nanomechanical characterization techniques, namely, atomic force microscope based PeakForce quantitative nanomechanical mapping (PF-QNM) and nanoindentation-based dynamical mechanical analysis (nano-DMA), to compare the modulus and the viscoelastic properties of organic polymers used routinely in organic electronics. They quantitatively demonstrate that the semiconducting near-amorphous organic polymer indacenodithiophene-co-benzothiadiazole (C16-IDTBT) has a higher carrier mobility, lower modulus, and greater nanoscale modulus areal uniformity compared to the semiconducting semicrystalline organic polymer poly[2,5-bis(3-tetradecylthiophen-2-yl)thieno[3,2-b]thiophene] (C14-PBTTT). Modulus homogeneity appears intrinsic to C16-IDTBT but can be improved in C14-PBTTT upon chemical doping.

electronic polymers, have played a pivotal role in the development of flexible and printed electronics over the last two decades.^[1–3] Composed from rings and chains of carbon atoms, these materials sport a low mass density, as well as electronic, optical, and mechanical properties that are tailored through the chemical design of their constituent molecular units. Weak inter-chain van der Waals bonding within thin films of stacked conjugated organic polymers renders them soft, with intrinsically low Young's moduli several orders of magnitude smaller than conventional inorganic semiconductors such as silicon.^[4] These mechanical properties, coupled with a conjugated organic polymer's ability to transport both charges and ions through their matrix, have expanded their use in new research areas such as organic bioelectronics and neural recording.^[5–10]

Organic polymers such as poly(3,4-ethylenedioxythiophene) polystyrene sulfonate (PEDOT:PSS) are now a routine choice for flexible microelectrode array implants,^[11] and their incorporation is known to improve electrical measurements through lower electrode impedances and higher signal-to-noise ratios.


However, a recent nanoscale mechanical characterization of the PEDOT:PSS film elements used in such microelectrode arrays showed local variations over an individual probe, on a length scale of a couple of square micrometers.^[12,13] This variation was

1. Introduction

Conjugated semiconducting organic polymers and amorphous polymer dielectrics, jointly referred to in this work as organic

V. Panchal
Bruker UK
Banner Lane, Coventry CV4 9GH, UK

I. Dobryden, P. M. Claesson
KTH Royal Institute of Technology
School of Engineering Sciences in Chemistry, Biotechnology and Health,
Department of Chemistry, Division of Surface and Corrosion Science
Drottning Kristinas väg 51, Stockholm SE-100 44, Sweden

 The ORCID identification number(s) for the author(s) of this article can be found under <https://doi.org/10.1002/aelm.202101019>.

© 2021 The Authors. Advanced Electronic Materials published by Wiley-VCH GmbH. This is an open access article under the terms of the Creative Commons Attribution License, which permits use, distribution and reproduction in any medium, provided the original work is properly cited.

DOI: 10.1002/aelm.202101019

I. Dobryden
Experimental Physics, Division of Materials Science
Department of Engineering Sciences and Mathematics
Luleå University of Technology
Luleå SE-971 87, Sweden

U. D. Hangen
Bruker Nano GmbH
Dennewartstrasse 25, 52068 Aachen, Germany

D. Simatos, L. J. Spalek, I. E. Jacobs, D. Venkateshvaran
Cavendish Laboratory
University of Cambridge
JJ Thomson Avenue, Cambridge CB3 0HE, UK
E-mail: dv246@cam.ac.uk

G. Schweicher
Laboratoire de Chimie des Polymères, Faculté des Sciences
Université Libre de Bruxelles (ULB)
Boulevard du Triomphe, Brussels 1050, Belgium

down to the PSS-rich regions having a higher modulus, and the PEDOT-rich regions having a lower modulus. Insights such as this allow one to re-engineer the nanomechanical properties of the polymer elements within multielectrode arrays to ensure performance reproducibility across all electrodes in the device.

In this work, we quantify the nanomechanical properties, their spatial homogeneity, and the depth-dependent viscoelastic behavior of three well known organic electronic polymers having three different morphologies. These polymers have been successfully used in functional organic thin film transistors over the years. Their processing for device integration from solution as well as their electronic properties are well understood, and a characterization of their nanomechanical properties make them future-ready for applications in conjugated polymer-based micro and nanomechanical devices. The three polymers investigated here are, a) the semiconducting semicrystalline polymer poly[2,5-bis(3-tetradecylthiophen-2-yl)thieno[3,2-b]thiophene] abbreviated as C14-PBTTT,^[14,15] b) the semiconducting near-amorphous planar-backbone donor-acceptor co-polymer indacenodithiophene-co-benzothiadiazole abbreviated as C16-IDTBT,^[16–18] and c) the dielectric amorphous fluoropolymer Cytop-M from AGC Inc.^[19] Our study attempts to quantify nanomechanical texture on length scales spanning several tens of nanometers to several hundred nanometers in these polymers, as such dimensions are directly applicable within micromechanical resonators. **Figure 1a** shows the chemical structures of these three organic polymers. **Figure 1b** displays a cross-sectional schematic of the top-gate bottom-contact

organic thin film transistors measured in this work. These transistors use a Cytop-M dielectric with an active layer of either C14-PBTTT or C16-IDTBT. **Figure 1c** shows the typical transfer and output characteristics of a field-effect transistor based on C14-PBTTT. The saturation mobility extracted from these measurements at maximum bias is $0.1 \text{ cm}^2 \text{ V}^{-1} \text{ s}^{-1}$. **Figure 1d** shows the typical transfer and output characteristics of a field-effect transistor based on C16-IDTBT. The saturation mobility extracted from these measurements at maximum bias is $1 \text{ cm}^2 \text{ V}^{-1} \text{ s}^{-1}$.

Although the micromechanical properties of C14-PBTTT were estimated using buckling metrology several years ago, the technique operated on the scale of hundreds of microns and was thus unable to differentiate between the intra-grain Young's modulus and the grain boundary Young's modulus within the film.^[20] In our effort to better understand the nanomechanical properties of the individual layers in organic field-effect transistors, we use high-resolution PeakForce quantitative nanomechanical mapping (PF-QNM) of the Young's modulus to demonstrate nanomechanical property variations in thin films of the semicrystalline polymer C14-PBTTT.^[21–23] We compare these semicrystalline nanomechanical properties with those of the near-amorphous low backbone torsion polymer semiconductor C16-IDTBT, and with the amorphous polymer dielectric Cytop-M. Cytop-M is routinely deployed as a gate dielectric within organic thin film transistors as shown in **Figure 1**. Unlike C14-PBTTT, both C16-IDTBT and Cytop-M have a smooth topography and show greater mechanical

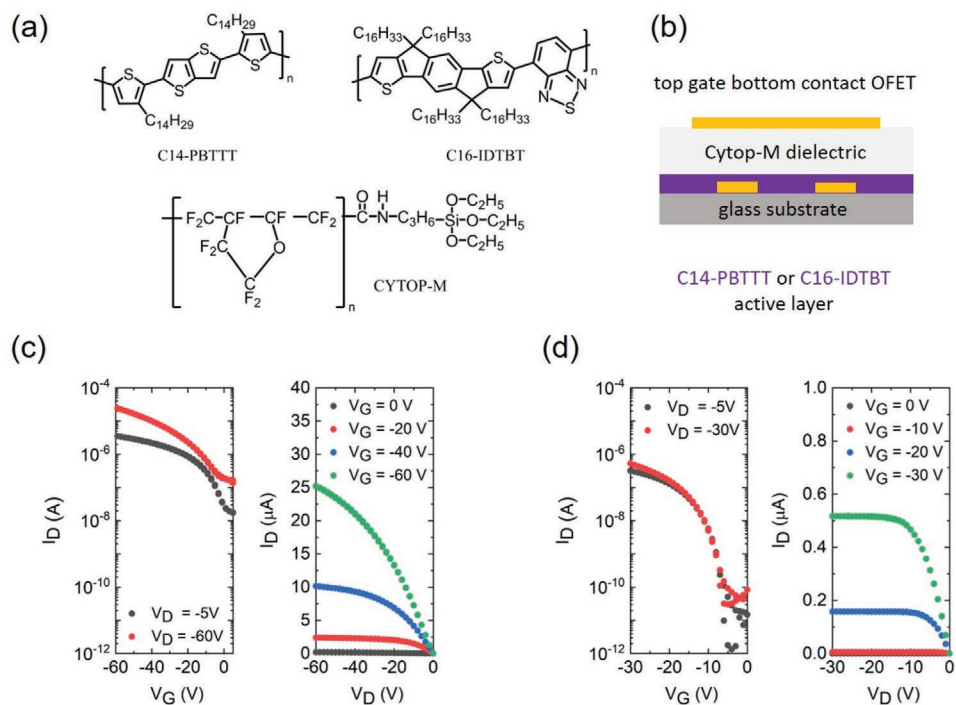


Figure 1. a) Chemical structures of the semicrystalline conjugated organic polymer C14-PBTTT, the near-amorphous conjugated organic polymer C16-IDTBT, and the amorphous fluorinated polymer Cytop-M. b) Cross-sectional schematic of a bottom-contact top-gate organic field-effect transistor architecture. c) Transfer and output characteristics of a C14-PBTTT based field-effect transistor with a Cytop-M dielectric. The channel length and width in this organic transistor was $L = 20 \mu\text{m}$ and $W = 1 \text{ mm}$, respectively. d) Transfer and output characteristics of a C16-IDTBT based field-effect transistor with a Cytop-M dielectric. The channel length and width in this organic transistor was $L = 120$ and $W = 40 \mu\text{m}$, respectively. The thin films of C14-PBTTT, C16-IDTBT, and Cytop-M were 50, 45, and 500 nm thick, respectively.

uniformity on the nanoscale. We finally use nanoindentation-based nanoscale dynamical mechanical analysis (nano-DMA) to draw up a comparison between the viscoelastic properties of the three organic polymers in question. The significant differences that we observe in the magnitude and nanoscale homogeneity of the mechanical properties in these materials provide crucial insights for the design of ultra-small polymer semiconductor based mechanical resonators.

2. Experimental Probes of Organic Polymer Nanomechanics

The atomic force microscope (AFM) based quantitative nanomechanical mapping of the Young's modulus, the adhesion and the deformation were performed using Bruker's Dimension IconXR. The measurements were performed with PeakForce Tapping based quantitative nanomechanical mapping (at 2 kHz) together with a laser Doppler vibrometer factory calibrated AFM probe with 30 nm tip radius and spring constant of 42.8 N m^{-1} (RTESPA-300-30), which are designed specifically for nanomechanical measurements. During the nanomechanical property mapping, the scan rate was set to 0.4 Hz, the PeakForce setpoint was 50 nN, and the scan area was set to $5 \mu\text{m} \times 5 \mu\text{m}$ or $1 \mu\text{m} \times 1 \mu\text{m}$ with 512×512 pixels. The imaging time took ≈ 20 min per scan. Before and after the measurements on the organic polymer samples presented in this study, the Dimension IconXR AFM was used to measure a reference sample of PDMS to confirm its known properties (see Section S1, Supporting Information). The reduced Young's moduli (E^*) reported in this work are extracted for every single pixel of the modulus maps by fitting the retract part of the force curve using the DMT model, $F_{\text{tip}} = \frac{4}{3} E^* \sqrt{Rd^3} + F_{\text{adh}}$, which takes into account the force on the tip (F_{tip}), the tip-sample adhesion force (F_{adh}), tip end radius (R), and tip-sample separation (d).^[21–23]

Additional confirmatory nanomechanical measurements were carried out on semicrystalline C14-PBTTT samples using a Dimension FastScan AFM (Bruker, USA). The measurements were conducted using a Tap300DLC probe with a diamond-like carbon tip coating. The actual spring constant, calibrated with the thermal calibration method, was 54.3 N m^{-1} . The tip outer radius was evaluated using a titanium roughness sample (RS-12M) and was ≈ 9 – 10 nm. The PeakForce setpoint was set to 98 nN. The scan rate in this case was 1.88 Hz.

Since confinement and nanostructuring are known to impact the measured mechanical properties of organic polymers, it is crucial to specify the thickness of the organic polymer films when specifying their measured modulus.^[24] In this study, the thickness of the three organic electronic polymers were chosen in keeping with their routine deposition parameters and dimensions used in organic field-effect transistors. The thin films of C14-PBTTT, C16-IDTBT, and Cytop-M reported here were 50, 45, and 500 nm thick, respectively. The thickness was estimated using a combination of an AFM and a DektakXT stylus profilometer. The error on these measurements was $\approx 5\%$. The organic thin films were spin-coated from solution onto very low surface roughness Si/SiO₂ substrates. Since the methods used to deposit the films also affect the measured elastic

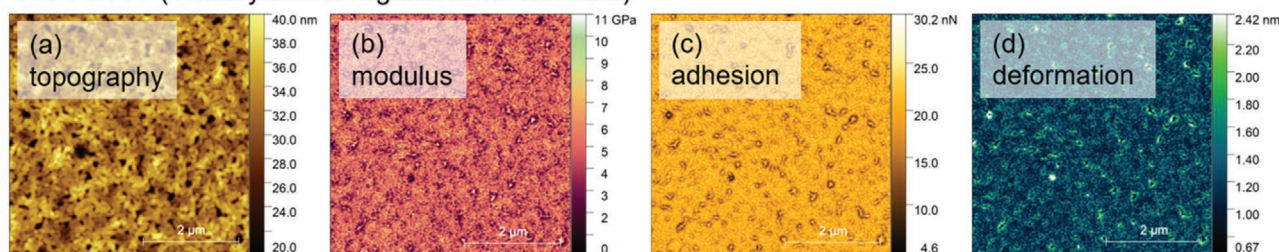
properties,^[25,26] it is also important to connect the measured values with the chosen film growth procedures (see Section S2, Supporting Information).

The topography, modulus, adhesion, and deformation documented in this work were extracted from the measured force curves between the AFM cantilever tip and the sample surface during measurement and plotted using the Gwyddion software with little to no data post-processing. Other than selecting a color palette and choosing an appropriate scale bar, no post-processing was done on the maps of the modulus, adhesion, and deformation. A correction to the modulus map was made to remove artefacts arising from horizontal line scanning only if necessary. Such minimal data surgery ensures a high level of data integrity as well as an ability to draw comparisons across the three polymers with confidence. In the case of the topography alone, Gwyddion's Align Rows feature was used with the median method to remove artefacts related to line scanning.

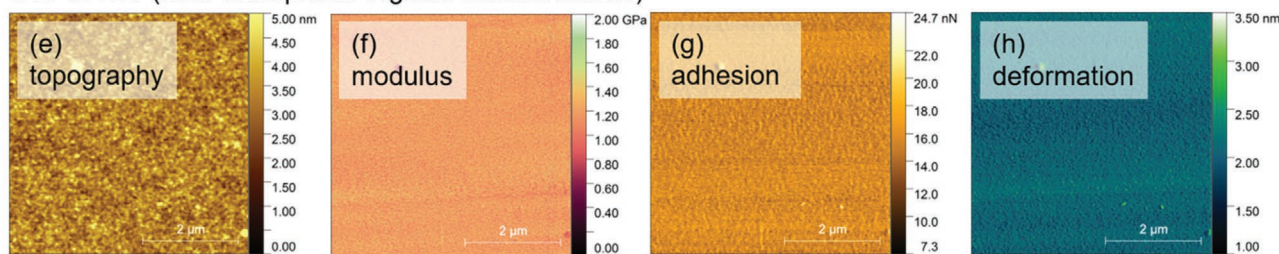
Nanoindentation-based nano-DMA on the three polymer films was performed using Bruker's Hysitron TI 980 TriboIndenter equipped with a Performech II controller. The thin film samples were mechanically clamped to the Hysitron stage without the need for additional sample preparation. The indentation experiments were performed using a cube corner indenter, the sharp geometry of which allows deforming a minimum sample volume to avoid substrate effects on the thin film measurement. Seeing as some of the organic films studied here are only ≈ 50 nm thick, the measurements using the TriboIndenter are done close to the instrument's working limits on sample thickness. The indentation tests shown in this work were performed with a standard 10 mN nano-DMA III transducer, but the actual load applied on the soft surface was typically only a few μN . During a nano-DMA examination, a relatively small sinusoidal load is superimposed over the quasi-static load applied to the probe. The resulting sinusoidal displacement signal-associated phase lag, together with the transducer calibration, are used to calculate the stiffness (k_s) and damping of the sample (C_s). Once the stiffness and damping of the materials are known, the dynamic moduli E' and E'' as well as $\tan \delta$ are calculated according to the equations, $E' = \frac{k_s \sqrt{\pi}}{2\sqrt{A}}$,

$E'' = \frac{\omega C_s \sqrt{\pi}}{2\sqrt{A}}$ and $\tan \delta = \frac{\omega C_s}{k_s}$. The storage modulus, E' , is the in-phase or real component of the modulus while the loss modulus, E'' , is the out-of-phase or imaginary component. E' describes the material's elastic response while E'' describes the material's viscous response. In the equations, A is the projected contact area and ω is the angular oscillation frequency. $\tan \delta$ is simply the ratio of the two dynamic moduli. We performed the dynamic indentation experiments at 20 Hz with a dynamic amplitude of 2 nm and the film properties were determined at small penetration depths of few nanometers. The stiff Si/SiO₂ substrates used reduces the displacement amplitude at larger depths, increasing the scattering in the measured parameters E' , E'' , and $\tan \delta$. Small penetration depths are necessary to avoid the limitations of pile-up which inadvertently affect the use of the Oliver Pharr procedure to estimate the modulus through indentation measurements on polymers.^[27]

C14-PBTTT (semicrystalline organic semiconductor)



C16-IDTBT (near-amorphous organic semiconductor)



Cytop M (amorphous organic dielectric)

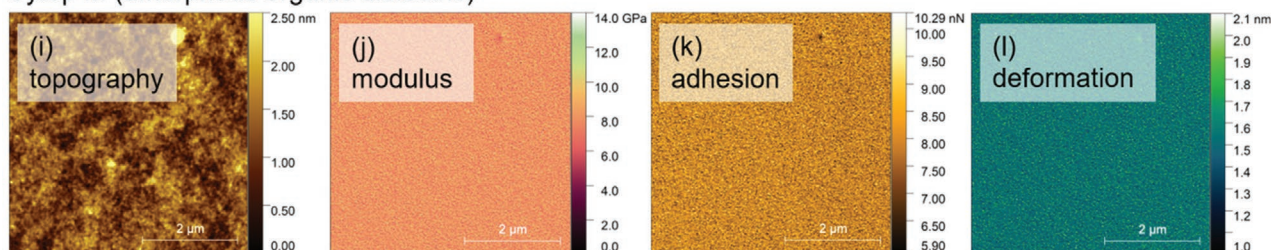


Figure 2. Topography, modulus, adhesion, and deformation in three organic electronic polymers, namely, C14-PBTTT (a–d), C16-IDTBT (e–h), and Cytop-M (i–l).

3. Results and Discussion

The nanomechanical properties of the organic electronic polymers measured using PF-QNM and their viscoelastic properties measured using nanoindentation are described in succession below.

3.1. PeakForce QNM Based Nanomechanical Characterization

Spatial maps of the topography, modulus, adhesion, and deformation over a $5 \mu\text{m} \times 5 \mu\text{m}$ scan area in C14-PBTTT, C16-IDTBT, and Cytop-M measured using PF-QNM are shown in **Figure 2**. As seen in this materials overview figure, large terraces of C14-PBTTT with voids in between the crystallites are evident from its topography. The modulus of C14-PBTTT follows these crystallites and displays significant non-uniformity. On the other hand, both the near-amorphous C16-IDTBT and the amorphous Cytop-M have smooth surfaces and show a high level of uniformity in their maps of topography and modulus at the current image resolution and scanned image size. The average values of the topographical roughness and modulus, together with the adhesion and deformation for the three different polymers are tabulated in **Table 1** together with their

RMS variations. C16-IDTBT and Cytop-M show an RMS topographical roughness $<0.55 \text{ nm}$. C14-PBTTT on the other hand is significantly rougher. The measured average modulus over the scan area of $5 \mu\text{m} \times 5 \mu\text{m}$ was 4.8 GPa for C14-PBTTT but came with a much greater RMS variation of nearly 30% in comparison with C16-IDTBT and Cytop-M. C16-IDTBT was the softest material of the three polymers with an average modulus of only 1.2 GPa , accompanied by a very high spatial uniformity as seen in its RMS variation of less than 10% the average value. The measured softness in the C16-IDTBT films is reflected in relatively larger values of the surface deformation of the film. Cytop-M shows the highest average modulus of the three polymers with a spatial uniformity larger than C14-PBTTT but

Table 1. Average values of roughness, modulus, adhesion, and deformation in the three organic electronic polymers, C14-PBTTT, C16-IDTBT, and Cytop-M measured over $5 \mu\text{m} \times 5 \mu\text{m}$.

Polymer	RMS roughness [nm]	Modulus [GPa]	Adhesion [nN]	Deformation [nm]
C14-PBTTT	3.21	4.80 ± 1.29	19.33 ± 2.36	1.25 ± 0.23
C16-IDTBT	0.55	1.17 ± 0.13	15.67 ± 1.43	2.07 ± 0.17
Cytop-M	0.39	7.91 ± 1.02	7.99 ± 0.71	1.53 ± 0.11

significantly smaller than C16-IDTBT. The adhesion of the three polymers C14-PBTTT, C16-IDTBT, and Cytop-M shows a trend that decreases jointly with the degree of crystallinity and the level of roughness in the film, with the rough semicrystalline sample C14-PBTTT having the highest adhesion and the amorphous flat Cytop-M sample having the lowest adhesion. Accurate estimates of the surface adhesion in these polymers are contingent on a complete removal of any residual solvent in the film prior to measurement.

Previous studies on polythiophenes such as C14-PBTTT have shown that a higher crystallinity within the organic polymer film leads to both a higher charge carrier mobility as well as a larger modulus.^[20] This intuitive relationship between the crystallinity, charge carrier mobility, and modulus, is not immediately apparent in C16-IDTBT and is discussed further below.

Both C14-PBTTT and C16-IDTBT have high charge carrier mobilities approaching $1 \text{ cm}^2 \text{ V}^{-1} \text{ s}^{-1}$,^[16,28,29] although the underlying charge transport mechanisms are different in the two materials. C14-PBTTT is ordered within its semicrystalline regions, with interdigitated alkyl side chains that enhance structural rigidity to facilitate charge transport along the π - π stacking direction in addition to transport along the twisted polymer backbone.^[28] In the case of C16-IDTBT however, its ultralow backbone-torsion permits fast transport along the polymer spine that is not impeded by the lack of alkyl side chain order.^[16] This is fundamentally why the two materials sport very different morphologies but still possess appreciable charge carrier mobilities. To help connect this existing picture with the mechanical properties of the two polymers, **Figure 3** shows high-resolution data on the topography and modulus maps over an area of $1 \mu\text{m}^2$ for semicrystalline C14-PBTTT

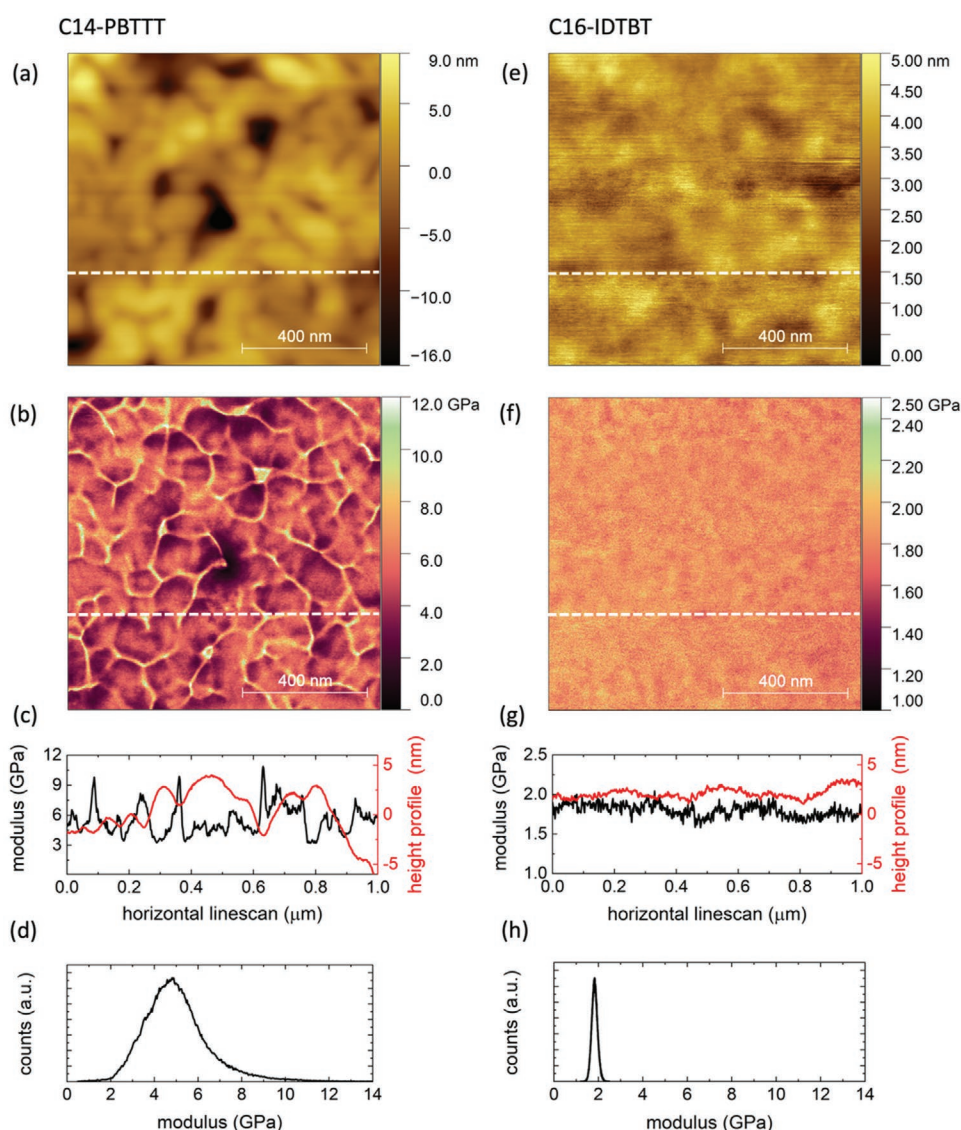


Figure 3. (a–d) are the topography, modulus, modulus, and topographical line scans along the dotted white lines, and modulus histogram over $1 \mu\text{m} \times 1 \mu\text{m}$, in C14-PBTTT respectively. (e–h) are the topography, modulus, modulus, and topographical line scans along the dotted white lines, and modulus histogram over $1 \mu\text{m} \times 1 \mu\text{m}$, in C16-IDTBT respectively.

and for near-amorphous C16-IDTBT. Figure 3a maps the individual grains and grain boundaries between the crystallites in C14-PBTTT. In Figure 3b, the corresponding spatial modulus is plotted, demonstrating clearly that the uniformity is broken at the grain boundaries. The same is visualized in Figure 3c which plots a line scan along the dotted white line of Figure 3b. Figure 3c also includes a line scan of the height topography, shown in red, along the white dotted line of Figure 3a showing that the modulus peaks at the topographical grain boundaries. The significant difference in the line scans of the topography and the modulus in Figure 3c is additional confirmation that the measured features are not influenced by the tip itself. Figure 3d plots a histogram of the moduli measured over the 512×512 pixels covering the area of $1 \mu\text{m}^2$. The measured average modulus is 5.1 ± 1.6 GPa but displays large variations across the area as seen through the width of the histogram. These properties are in stark contrast to the topography and modulus of C16-IDTBT shown in Figures 3e and 3f, respectively. The topographical image clarity depends on the type of probe used, its radius, the surface force applied, and the dimension of the features on the film. Using the current cantilever tip with tip radius of 30 nm (designed primarily for nanomechanical measurements and hence stiffer than conventional AFM probes), the topography appears blurry on scanned areas of a square micron and under. This is on account of limited lateral resolution, but also because the C16-IDTBT surface is very smooth. It has a topographical roughness much smaller than the deformation on the surface during measurement. The soft surface is hence potentially flattened during the measurement. One should keep in mind that the topography and the modulus are coupled in these measurements as they are quantities read out from the same force curve. The topographical scans shown in this work are for the case where large forces are applied to the surface, as opposed to conventional AFM measurements that do not require simultaneous surface indentation. Under these conditions and at high-resolution, these films are smooth, and show little spatial variation in the modulus. A modulus line scan along the white dotted line of Figure 3f is shown in Figure 3g together with its accompanying topographical line scan. This line scan demonstrates a high level of lateral uniformity in the modulus, even though the topography registers a broader undulation. The fact that the grain size of C16-IDTBT is well below the diameter of the cantilever tip,^[30] places a limit on the nanoscale variations that can be imaged using our current setup, and on the length scale that we report uniformity over. Figure 3h documents the comparably narrow modulus histogram of C16-IDTBT over the $1 \mu\text{m}^2$ scanned area, demonstrating little spatial variation with an average value of 1.8 ± 0.1 GPa. Despite being smooth and near-amorphous, the width of the modulus histogram for C16-IDTBT is well below that of Cytop-M, which is fully amorphous but comparatively smooth (see Section S3, Supporting Information).

On first assessment, it may seem as though the modulus values measured on the $1 \mu\text{m}^2$ areas are larger than those measured on $5 \mu\text{m} \times 5 \mu\text{m}$ areas (Figure 2 and Table 1). In the case of C14-PBTTT, the modulus values agree within the error bars. In the case of C16-IDTBT on the other hand, the average modulus goes from 1.2 GPa measured over $5 \mu\text{m} \times 5 \mu\text{m}$ to 1.8 GPa measured over $1 \mu\text{m} \times 1 \mu\text{m}$. An additional measurement that

we performed on an area of $5 \mu\text{m} \times 2.5 \mu\text{m}$ a week earlier to that documented in Figure 1, but which again confirmed the spatial homogeneity (narrow modulus histogram) on the probed length scales in C16-IDTBT showed an average modulus value of 2 GPa (see Section S4, Supporting Information). Repeated measurements on several areas in various C16-IDTBT films have confirmed that the value of its nanoscale modulus, measured a few weeks after fabrication and upon ambient air exposure, sits between 1 and 2 GPa. The narrow modulus histogram in C16-IDTBT remains a universal feature in the repeated measurements.

Improved spatial homogeneity in the modulus of the semicrystalline polymer C14-PBTTT can be achieved upon chemical doping. A recent study on the semiconducting polymer P3HT, containing both amorphous and crystalline domains, showed that chemical doping tends to soften the crystalline domains.^[31] The doped crystalline domains in P3HT show a reduced modulus, and their co-existence with amorphous domains in the film causes the spatial modulus histogram in doped P3HT to show a double peak feature.^[31] C14-PBTTT films have large semicrystalline terraces, and when chemically doped, shows a spatial modulus histogram that has a single peak. Figure 4a shows a comparison of the spatial modulus measured on a pristine C14-PBTTT film compared with a C14-PBTTT film that was chemically doped to high conductivities up to 1000 S cm^{-1} using an ion exchange based doping process (see Section S5, Supporting Information).^[32] The pristine C14-PBTTT film has a low conductivity of $\approx 10^{-5} \text{ S cm}^{-1}$ at low lateral bias and under no applied gate voltage. This intrinsic value is on account of C14-PBTTT's unintentional doping in oxygen. The diminished contrast in the measured modulus within the doped C14-PBTTT film shows that the individual domains are uniformly reduced in the average modulus. Doping also leads to a reduction in the modulus at the grain boundaries, as seen in Figure 4b that compares modulus line scans in pristine C14-PBTTT with doped C14-PBTTT along the white dotted lines of Figure 4a. Figure 4c compares the spatial modulus histograms of pristine C14-PBTTT, doped C14-PBTTT, and C16-IDTBT. In addition to a reduced average modulus of 3.36 ± 1.03 GPa, doping of semicrystalline C14-PBTTT also leads to higher spatial uniformity, reflected in a narrower width of the modulus histogram. Although this represents an improvement over pristine C14-PBTTT, the homogeneity is still less than that measured in C16-IDTBT. C16-IDTBT cannot be efficiently doped using the same ion exchange procedure on account of its near-amorphous character. The cause for a reduced modulus in C14-PBTTT upon doping may be down to a few factors. One factor accounts for an expansion of the lamellae upon dopant incorporation within the film, which reduce alkyl side chain van der Waals interactions and reduce the attractive Coulombic interaction between planes of dopant ions and polarons.^[32] A second factor may be down to a small number of residual solvent molecules that are incorporated in the film during the ion-exchange doping procedure.

In performing the nanomechanical measurements on C14-PBTTT and on C16-IDTBT, we processed the films using our optimized protocol that ensures high charge carrier mobilities within field-effect transistors.^[16,28] Devices made from C14-PBTTT are known to show high mobilities immediately

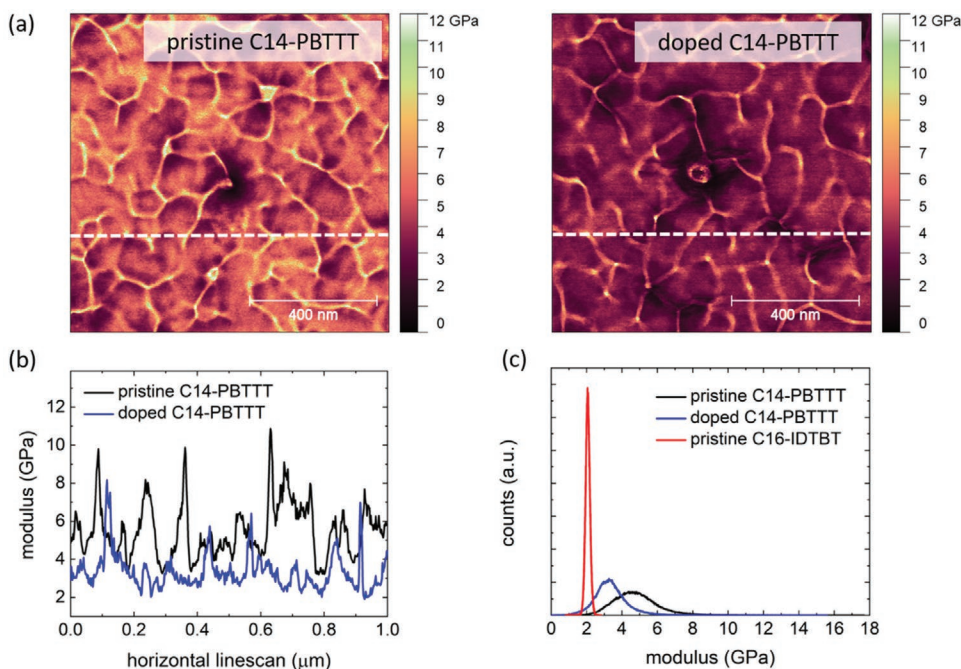


Figure 4. a) Comparison between the areal modulus over $1 \mu\text{m} \times 1 \mu\text{m}$ in pristine C14-PBTTT and in doped C14-PBTTT, b) modulus line scans along the dotted white lines in pristine C14-PBTTT and in doped C14-PBTTT, and c) comparison between the modulus histograms measured over $1 \mu\text{m} \times 1 \mu\text{m}$ in pristine C14-PBTTT, in doped C14-PBTTT and in C16-IDTBT.

after fabrication but degrade over a span of days to weeks upon air exposure.^[15,28,33,34] The degradation of C14-PBTTT in air is seen through a gradually diminishing on-current, a gradually reducing mobility, and an increasing off-current in transistors fabricated from it.^[15,28,33,34] C16-IDTBT on the other hand, requires a few days of air exposure to stabilize its high mobility after which it remains air stable for months.^[35] Hence, to probe the nanomechanical properties of C14-PBTTT and doped C14-PBTTT in their high mobility configuration, the measurements on them were carried out within the first week from fabrication. The measurements on C16-IDTBT on the other hand, were measured a few weeks after fabrication to allow sufficient time for the polymer film to stabilize its electronic properties in air. This process ensures that trap healing in C16-IDTBT is complete within the film at the time of estimating its modulus (see Section S6, Supporting Information). A comprehensive study on how the mechanical properties in C14-PBTTT age when left in air over several weeks is an investigation that goes beyond the current work. This said, preliminary measurements hint at there being a modest change in C14-PBTTT after several weeks (see Sections S7 and S8, Supporting Information). This change potentially accompanies its electronic degradation over the same period. The role of humidity upon air exposure in these films is not known at this time, but detrimental effects have been observed previously in organic–inorganic semicrystalline films where the degradation mechanism begins at the grain boundaries.^[36,37] All told, the fact that C16-IDTBT sports a high mobility despite its near-amorphous morphology in addition to a spatially homogeneous modulus that is comparatively low, makes this donor–acceptor co-polymer semiconductor a candidate for truly flexible organic microelectronics and electro-mechanical devices.^[38]

3.2. TriboIndenter-Based Nanoscale Viscoelastic Property Characterization as a Complementary Characterization Tool to PeakForce QNM

Nanoindentation based mechanical measurements complement the mechanical properties determined by AFM-based PF-QNM. Although the contact mechanics between the tip and the sample are similar in both approaches, the sensor characteristics are different. An exploration of a larger field of parameters can thus be made by employing both techniques side by side. The larger dimension of the indenter in nanoindentation permits its force and displacement measurement to be calibrated utilizing standards from NIST which remain even when tips are changed. The tips are typically manufactured from diamond and their shape remains unchanged upon tip cleaning. A nanoindenter (NI) has built-in routines to calibrate a complex (non-spherical) tip including its apex and its pyramid base described by a 6-parameter area function. The nanoindenter tip is mounted on a stylus and typically penetrates the tested material while the AFM tip is mounted on a cantilever and operates in a regime of elastic deformation of the sample surface. While a sharp tip is advantageous for both instruments to reduce the adhesion forces when in contact and obtain high spatial resolution maps, a blunt tip radius is necessary for accurate mechanical measurements to focus on the repulsive forces of the surface. A small sideways motion of the tip on an AFM cantilever could be a concern for large deformations, however in nanoindentation, the tip dragging laterally on the surface is $<0.5 \text{ nm}$, out of the 60 nm vertical motion. Characteristic differences between the nanoindenter and the AFM used in this work are summarized in Table 2.

Table 2. Comparison between the salient characteristics of nanoindentation and AFM.

Parameter	Nanoindentation	AFM
Tip radius	50 nm	30 nm
Frequency range	0.1–300 Hz	0.1 Hz to 6 MHz
Force noise floor	30 nN	Few piconewtons
Max force during experiment	Few micronewtons	80 nN

Bruker's TI 980 nanoindenter used in the present experiments was equipped with a sharp diamond indenter tip with a cube corner geometry and a radius of ≈ 50 nm. The tip shape was calibrated by routines described in the instrument's user manual and in ISO14577 for the depth range between 5 and 150 nm. Indentation experiments were performed on virgin positions of each polymer sample. The tip oscillated at a frequency of 20 Hz with an amplitude of ≈ 2 nm while approaching the sample. The surface of the sample was determined at the displacement position at which the contact stiffness began rising. The amplitude and phase of the oscillation was measured by a lock-in amplifier and then analyzed following earlier work.^[39–41]

The mechanical properties of the polymers investigated in this work, determined as a function of penetration depth, are shown in **Figure 5**. The properties of the thin polymer films on the hard substrate can be discussed starting from a penetration depth of 5 nm—the lower end of calibration of the tip shape. The sharp cube corner indenter allows measuring the properties of the polymer without a pronounced substrate effect

and the film properties of each sample should be read from the plateau region starting above 5 nm. The hardness peak at low penetration depth is often called skin effect—attributing higher properties to the surface skin of polymers—there are however other effects to be considered before the observation can be attributed to a different cross-linking of polymers in the skin. Hardness is understood as the average stress in the contact zone and can be overestimated because the adhesive forces that act in the contact zone are not fully measurable with the indenter-force-sensor. Moreover, the material experiences the highest strain rates at the initial penetration depth and a strain rate sensitive polymer requires higher stresses to be deformed at higher strain rates. The measured nanomechanical parameters using the indenter are typically lower than the measurements performed with the AFM. The difference is linked to the different frequency regime of testing namely, 2 kHz on the AFM versus 20 Hz on the nanoindenter. Nevertheless, at 20 Hz, the viscoelastic properties are probed with higher fidelity, as the polymer's tactile response upon slow tapping can be measured more accurately.

Figure 5a shows a comparison between the hardness of the polymers as a function of penetration depth studied under nanoindentation. The overall trend as measured by the AFM continues to be preserved in this regime of low tapping at 20 Hz, with the exception that the doped polymer C14-PBTTT is the least hard. The slight rise in the hardness of C16-IDTBT at higher penetration depths as seen in Figure 5a is possibly because the film retains more residual solvent in its bulk during processing, thus causing substrate effects to kick in earlier. Figure 5b–d shows a comparison between the viscoelastic

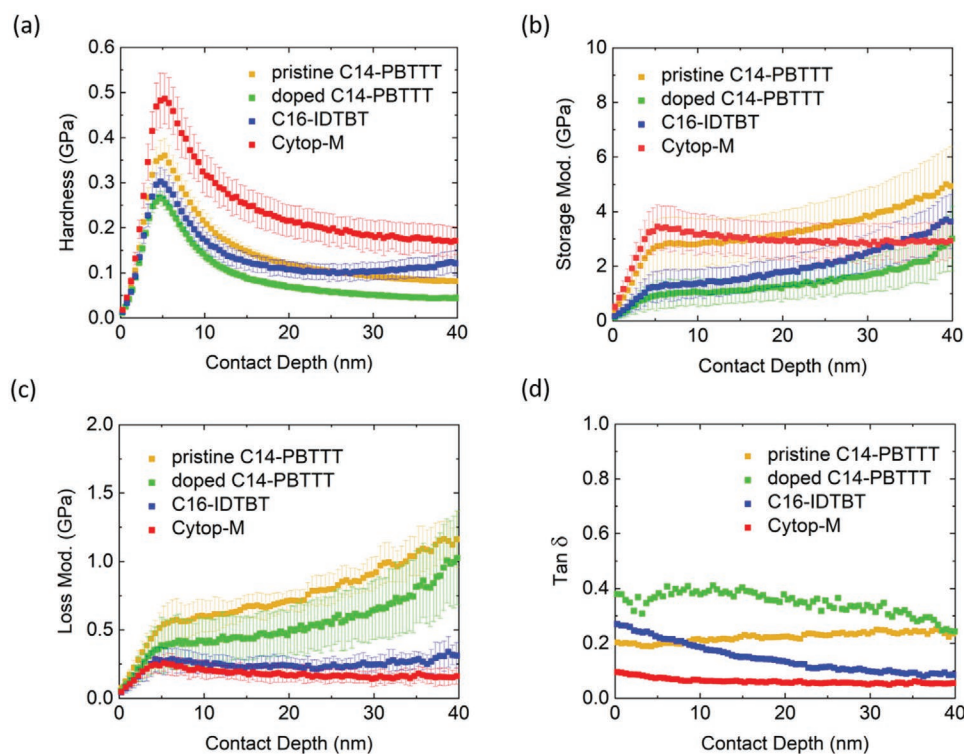


Figure 5. Nanoscale dynamical mechanical analysis of pristine C14-PBTTT, doped C14-PBTTT, C16-IDTBT and Cytop-M performed using Bruker's TI 980 TriboIndenter. a) Hardness, b) storage modulus, c) loss modulus, and d) $\tan \delta$.

properties, that is, the storage modulus, loss modulus, and the loss tangent, $\tan \delta$, of the polymers in question. Cytop-M, being an order of magnitude thicker than the other organic polymer films at a thickness of 500 nm, shows the most robust measured plateaus arguably because substrate effects do not kick in at these penetration depths. The loss tangent $\tan \delta$ is the highest for the doped C14-PBTTT film. This observation leads one to understand that although the doping process causes an increase in conductivity which is a positive for electrical applications, it is accompanied by higher viscoelastic/mechanical losses, a property that needs to be considered when deploying such doped polymers in mechanical resonators. Furthermore, a higher $\tan \delta$ at the surface of the doped C14-PBTTT film illustrates that the viscous response is more important at low contact depths than it is for pristine C14-PBTTT. Since the $\tan \delta$ curves for pristine C14-PBTTT and doped C14-PBTTT approach each other at higher contact depths, it appears that the bulk is not affected to the same extent by doping, or that substrate effects are observed. The reduction in the $\tan \delta$ of C16-IDTBT as a function of contact depth suggests that the indenter probe squeezes the film, displacing the residual solvent in the bulk under the probe in the process. This causes a reduction in the viscoelastic losses as the film is compacted under the probe tip.

In addition to film penetration, the nanoindenter was also used in its sensitive scanning probe microscopy mode to map the topographical differences between pristine C14-PBTTT and doped C14-PBTTT. Using this nanoindenter-based scanning probe microscopy mode, the topographical roughness as measured in the two films using the AFM were reconfirmed (see Section S9, Supporting Information).

4. Conclusions

Micromechanical and electromechanical devices built using organic electronic polymers necessitate a greater understanding of the active layer's mechanical properties on the grain-scale and the nanoscale. In this work, we use precision instrumentation techniques to compare the nanomechanical properties of organic polymers that commonly constitute the layers in a polymer thin film transistor. We contrast two well-known organic polymer semiconductors on the grounds of their mobility, morphology, modulus, modulus homogeneity, and their low-frequency viscoelastic response. Our study focuses primarily on quantifying nanomechanical texture on length scales spanning several tens of nanometers to several hundred nanometers, as these dimensions are directly applicable within micromechanical resonators. On said length scales, the high-mobility organic polymer C16-IDTBT shows a greater spatial homogeneity in its modulus compared with the high-mobility organic polymer C14-PBTTT. As C14-PBTTT can be chemically doped efficiently, we studied the influence of doping on the modulus and showed that the process is accompanied by a lower average modulus with improved spatial homogeneity compared to its pristine counterpart. Although doping increases the electrical conductivity of the film, its mechanical losses also increase. The latter is a finding that needs to be accounted for in electromechanical devices based on conductive organic polymers.

Supporting Information

Supporting Information is available from the Wiley Online Library or from the author.

Acknowledgements

D.V. acknowledges the Royal Society for funding in the form of a Royal Society University Research Fellowship (Royal Society Reference No. URF\R1\201590). D.V. is thankful to Henning Sirringhaus for having facilitated this work by providing a cleanroom and a nitrogen glovebox deposition facility to deposit the high purity organic thin films analyzed in this study. D.V. is also thankful to Iain McCulloch for having supplied C14-PBTTT and C16-IDTBT used in this work. D.S. acknowledges support from the Sensor CDT and the Engineering and Physical Sciences Research Council (Grant No. EP/L015889/1). G.S. acknowledges postdoctoral fellowship support from the Belgian National Fund for Scientific Research (FNRS).

Conflict of Interest

The authors declare no conflict of interest.

Author Contributions

V.P., I.D., and U.D.H. contributed equally to this work. V.P. and I.D. performed the PeakForce Quantitative Nanomechanical Mapping measurements on the three organic polymers using a Bruker Dimension IconXR AFM and a Bruker FastScan AFM. U.D.H. performed the viscoelastic characterization using Bruker's TI 980 TriboIndenter. D.S. and D.V. fabricated the organic polymer thin films and devices used in this study and engaged in regular discussions on the interpretation of the experimental measurements. L.J.S. acted as a sounding board for the ideas presented in the paper, engaged in regular discussions on the interpretation of the experimental measurements and provided regular critical feedback on the manuscript. G.S. and I.E.J. contributed to discussions and experimental work on the doping properties of organic semiconductors. P.M.C. and D.V. coordinated and supervised the collaboration between KTH Stockholm and the University of Cambridge. D.V. conceived the idea of measuring and comparing the nanoscale properties of organic semiconducting polymers and wrote the final manuscript together with U.D.H.

Data Availability Statement

The data that support the findings of this study are available from the corresponding author upon reasonable request.

Keywords

nanomechanics, organic electronics, organic field-effect transistors, organic semiconducting polymers, young's modulus

Received: September 22, 2021

Revised: October 27, 2021

Published online:

[1] S. Chung, K. Cho, T. Lee, *Adv. Sci.* **2019**, *6*, 1801445.

[2] U. Zschieschang, H. Klauk, *J. Mater. Chem. C* **2019**, *7*, 5522.

- [3] D. Corzo, G. Tostado-Blázquez, D. Baran, *Front. Electron.* **2020**, *1*, 594003.
- [4] S. E. Root, S. Savagatrup, A. D. Printz, D. Rodriguez, D. J. Lipomi, *Chem. Rev.* **2017**, *117*, 6467.
- [5] Y. Liu, J. Liu, S. Chen, T. Lei, Y. Kim, S. Niu, H. Wang, X. Wang, A. M. Foudeh, J. B.-H. Tok, Z. Bao, *Nat. Biomed. Eng.* **2019**, *3*, 58.
- [6] D. Khodagholy, J. N. Gelinás, T. Thesen, W. Doyle, O. Devinsky, G. G. Malliaras, G. Buzsáki, *Nat. Neurosci.* **2015**, *18*, 310.
- [7] J. E. Chung, H. R. Joo, J. L. Fan, D. F. Liu, A. H. Barnett, S. Chen, C. Geaghan-Breiner, M. P. Karlsson, M. Karlsson, K. Y. Lee, H. Liang, J. F. Magland, J. A. Pebbles, A. C. Tooker, L. F. Greengard, V. M. Tolosa, L. M. Frank, *Neuron* **2019**, *101*, 21.
- [8] K. A. Ludwig, J. D. Uram, J. Yang, D. C. Martin, D. R. Kipke, *J. Neural Eng.* **2006**, *3*, 59.
- [9] A. Carnicer-Lombarte, S.-T. Chen, G. G. Malliaras, D. G. Barone, *Front. Bioeng. Biotechnol.* **2021**, *9*, 622524.
- [10] Z. Ma, S. Li, H. Wang, W. Cheng, Y. Li, L. Pan, Y. Shi, *J. Mater. Chem. B* **2019**, *7*, 173.
- [11] E. Musk, Neuralink, *J. Med. Internet Res.* **2019**, *21*, e16194.
- [12] M. Sanviti, A. Alegria, D. E. Martínez-Tong, *ChemRxiv* **2021**, <https://doi.org/10.26434/chemrxiv.14135315.v1>.
- [13] L. Ouyang, C.-C. Kuo, B. Farrell, S. Pathak, B. Wei, J. Qua, D. C. Martin, *J. Mater. Chem. B* **2015**, *3*, 5010.
- [14] D. M. DeLongchamp, R. J. Kline, E. K. Lin, D. A. Fischer, L. J. Richter, L. A. Lucas, M. Heeney, I. McCulloch, J. E. Northrup, *Adv. Mater.* **2007**, *19*, 833.
- [15] I. McCulloch, M. Heeney, M. L. Chabinyc, D. DeLongchamp, R. J. Kline, M. Colle, W. Duffy, D. Fischer, D. Gundlach, B. Hamadani, R. Hamilton, L. Richter, A. Salleo, M. Shkunov, D. Sparrowe, S. Tierney, W. Zhang, *Adv. Mater.* **2009**, *21*, 1091.
- [16] D. Venkateshvaran, M. Nikolka, A. Sadhanala, V. Lemauro, M. Zelazny, M. Kepa, M. Hurhangee, A. J. Kronemeijer, V. Pecunia, I. Nasrallah, I. Romanov, K. Broch, I. McCulloch, D. Emin, Y. Olivier, J. Cornil, D. Beljonne, H. Sirringhaus, *Nature* **2014**, *515*, 384.
- [17] W. M. Zhang, J. Smith, S. E. Watkins, R. Gysel, M. McGehee, A. Salleo, J. Kirkpatrick, S. Ashraf, T. Anthopoulos, M. Heeney, I. McCulloch, *J. Am. Chem. Soc.* **2010**, *132*, 11437.
- [18] X. Zhang, H. Bronstein, A. J. Kronemeijer, J. Smith, Y. Kim, R. J. Kline, L. J. Richter, T. D. Anthopoulos, H. Sirringhaus, K. Song, M. Heeney, W. Zhang, I. McCulloch, D. M. DeLongchamp, *Nat. Commun.* **2013**, *4*, 2238.
- [19] D. Simatos, L. J. Spalek, U. Kraft, M. Nikolka, X. Jiao, C. R. McNeill, D. Venkateshvaran, H. Sirringhaus, *APL Mater.* **2021**, *9*, 041113.
- [20] B. O'Connor, E. P. Chan, C. Chan, B. R. Conrad, L. J. Richter, R. J. Kline, M. Heeney, I. McCulloch, C. L. Soles, D. M. DeLongchamp, *ACS Nano* **2010**, *4*, 7538.
- [21] T. J. Young, M. A. Monclus, T. L. Burnett, W. R. Broughton, S. L. Ogin, P. A. Smith, *Meas. Sci. Technol.* **2011**, *22*, 125703.
- [22] P. M. Claesson, I. Dobryden, G. Li, Y. He, H. Huang, P.-A. Thoren, D. B. Haviland, *Phys. Chem. Chem. Phys.* **2017**, *19*, 23642.
- [23] R. Garcia, *Chem. Soc. Rev.* **2020**, *49*, 5850.
- [24] S. E. Root, N. E. Jackson, S. Savagatrup, G. Arya, D. J. Lipomi, *Energy Environ. Sci.* **2017**, *10*, 558.
- [25] H.-C. Tien, Y.-W. Huang, Y.-C. Chiu, Y.-H. Cheng, C.-C. Chueh, W.-Y. Lee, *J. Mater. Chem. C* **2021**, *9*, 2660.
- [26] B. D. Vogt, *J. Polym. Sci. Part B: Polym. Phys.* **2018**, *56*, 9.
- [27] D. Tranchida, S. Piccarolo, J. Loos, A. Alexeev, *Macromolecules* **2007**, *40*, 1259.
- [28] I. McCulloch, M. Heeney, C. Bailey, K. Genevicius, I. MacDonald, M. Shkunov, D. Sparrowe, S. Tierney, R. Wagner, W. Zhang, M. L. Chabinyc, R. J. Kline, M. D. McGeehee, M. F. Toney, *Nat. Mater.* **2006**, *5*, 328.
- [29] J.-F. Chang, M. C. Gwinner, M. Caironi, T. Sakanoue, H. Sirringhaus, *Adv. Funct. Mater.* **2010**, *20*, 2825.
- [30] C. Cendra, L. Balhorn, W. Zhang, K. O'Hara, K. Bruening, C. J. Tassone, H.-G. Steinrück, M. Liang, M. F. Toney, I. McCulloch, M. L. Chabinyc, A. Salleo, C. J. Takacs, *ACS Macro Lett.* **2021**, *10*, 1306.
- [31] H. Maddali, K. L. House, T. J. Emge, D. M. O'Carroll, *RSC Adv.* **2020**, *10*, 21454.
- [32] I. E. Jacobs, Y. Lin, Y. Huang, X. Ren, D. Simatos, C. Chen, D. Tjhe, M. Statz, L. Lai, P. A. Finn, W. G. Neal, G. D'Avino, V. Lemauro, S. Fratini, D. Beljonne, J. Strzalka, C. B. Nielsen, S. Barlow, S. R. Marder, I. McCulloch, H. Sirringhaus, *Adv. Mater.* **2021**, *2102988*.
- [33] M. L. Chabinyc, R. A. Street, J. E. Northrup, *Appl. Phys. Lett.* **2007**, *90*, 123508.
- [34] P. Boufflet, Y. Han, Z. Fei, N. D. Treat, R. Li, D.-M. Smilgies, N. Stingelin, T. D. Anthopoulos, M. Heeney, *Adv. Funct. Mater.* **2015**, *25*, 7038.
- [35] M. Nikolka, I. Nasrallah, B. Rose, M. K. Ravva, K. Broch, A. Sadhanala, D. Harkin, J. Charmet, M. Hurhangee, A. Brown, S. Illig, P. Too, J. Jongman, I. McCulloch, J.-L. Bredas, H. Sirringhaus, *Nat. Mater.* **2017**, *16*, 356.
- [36] W.-C. Liao, B. H. Liu, C.-C. Leu, *Appl. Surf. Sci.* **2020**, *507*, 1450782.
- [37] I. Mela, C. Puudel, M. Anaya, G. Delpont, K. Frohna, S. Macpherson, T. A. S. Doherty, A. Scheeder, S. D. Stranks, C. F. Kaminski, *Adv. Funct. Mater.* **2021**, *31*, 2100293.
- [38] Y. Zheng, G.-J. N. Wang, J. Kang, M. Nikolka, H.-C. Wu, H. Tran, S. Zhang, H. Yan, H. Chen, P. Y. Yuen, J. Mun, R. H. Dauskardt, I. McCulloch, J. B.-H. Tok, X. Gu, Z. Bao, *Adv. Funct. Mater.* **2019**, *29*, 1905340.
- [39] S. A. S. Asif, K. J. Wahl, R. J. Colton, *Rev. Sci. Instrum.* **1999**, *70*, 2408.
- [40] S. A. S. Asif, K. J. Wahl, R. J. Colton, *J. Mater. Res.* **2000**, *15*, 546.
- [41] S. A. S. Asif, K. J. Wahl, R. J. Colton, O. L. Warren, *J. Appl. Phys.* **2001**, *90*, 1192.